Description of A Nine–Level Grid Point Atmospheric General Circulation Model

*Liang Xinzhong*① (梁信忠)
Institute of Atmospheric Physics, Chinese Academy of Sciences, Beijing 100080
Received March 1, 1996

ABSTRACT

A brief description of a nine–level grid–point global atmospheric general circulation model is presented with the emphasis on the physics parameterizations. This model was developed by the modeling group from Institute of Atmospheric Physics as one task of the CO_2–Climate cooperation project between Chinese Academy of Sciences and United States Department of Energy. The task was initiated by Qing–Cun Zeng (IAP) and Robert D. Cess (SUNY). The operational design, computer coding and climate simulation tuning of the model were mainly carried out by Xue–Hong Zhang (for dynamics) and the author (for physics) in SUNY at Stony Brook. The final version was frozen in September 1990. Preliminary diagnoses showed that the model reproduces principal features of the observed climatology.

key words: Atmospheric General Circulation Modlel, Physics parameterizations

I. INTRODUCTION

On the basis of systematic investigations in the fields of numerical weather prediction and computational geophysical fluid dynamics, Zeng (1983) designed a unified numerical model that describes the fully coupled atmosphere–ocean general circulation system, i.e., IAP GCM. The first operational model of this design was the two–level atmospheric GCM and developed through team efforts (Liang 1986; Zeng et al. 1987, 1989). This two–level model demonstrates long–term computational stability and reasonable global climate simulation capability (Liang 1986) and has been widely used as a basic numerical tool for scientific and educational studies of global climate and variations in Chinese research institutes and universities.

The application of the two–level IAP AGCM is, however, limited by its insufficient vertical resolution and outdated physics representation. The earth's atmospheric vertical structure is much more complex than that can be described by two levels. It is necessary to develop a multi–level model that incorporates the most recent developments of physics representation. As a first attempt in 1987, the development of a nine–level model with its top at 10 hPa was initiated by Qing–Cun Zeng (IAP) and Robert D. Cess (SUNY) to be carried as one task of the CO_2–Climate cooperation project between Chinese Academy of Sciences and United States Department of Energy. To fulfill the task, Xue–Hong Zhang and the author were invited as visiting scholars in SUNY at Stony Brook during 1987–1990.

①Current affiliation: Atmospheric Sciences Research Center, State University of New York at Albany, NY 12205.

The operational design and computer coding of the model dynamics (the dry, non-dissipative and adiabatic atmosphere) were fulfilled by Xue-Hong Zhang in 1988. As a historical descendant of the two-level IAP AGCM (Zeng et al., 1989), the nine-level model uses the finite-difference scheme that conserves the "available" energy in the C-grid spherical-coordinate system (Zeng, 1983). The same horizontal resolution, i.e., 4° latitude by 5° longitude, is adopted while the model top is extended from 200 hPa upward to 10 hPa. Since the dynamical module was well documented by Zhang (1990), Section 2 describes only the modifications by the author, which are necessary to achieve a consistent coupling with the model physics.

To match the vertical resolution increase, the entire physics representation of the model was newly designed and developed by the author during 1987-1989. This physical module includes major atmospheric processes such as convection, precipitation, cloud formation, radiation, eddy diffusion, gravity-wave drag, and surface-atmosphere interaction. A brief description of these components is given in Section 3. The model requires the prescription of several surface boundary conditions including geographical distributions of terrain elevation, sea surface temperature, sea ice, vegetation type, soil texture and soil color, and the determination of surface albedo, emissivity, roughness and soil properties. These were prepared by the author in 1988 and described in Section 4. Finally, Section 5 presents preliminary results of the model climate simulation, which was conducted using the froze version in September 1990.

II. THE MODEL DYNAMICS

A detailed description of the dynamical module was documented by Zhang (1990). To achieve a consistent coupling with the model physics, several modifications to the default module were performed. Two major changes are described below.

First, Smagorinsky-type non-linear horizontal diffusion of heat, momentum and moisture, Arakawa-type high-latitude filter and Shapiro-type spatial smoothing were added to enhance the computational stability and improve the model climate simulation capability. These schemes were the same as in the two-level model and well described by Liang (1986).

Second, the moisture prediction was added so that the hydrological cycle can be properly represented. The temporal and spatial distributions of moisture determine many important processes such as condensation / precipitation, cloud-radiation interaction and surface-atmosphere energy redistribution. Extreme care is needed to predict variations of moisture because of its positive definite nature. Here the moisture transport is predicted by the multidimensional positive definite advection transport algorithm (Smolarkiewicz and Grabowski, 1990). This scheme is nonoscillatory with small diffusion so that it predicts positive definite quantity with high accuracy. Detail modifications were taken to implement this scheme into the C-grid spherical-sigma coordinate system.

III. THE MODEL PHYSICS

When a comprehensive documentation for the representation of a specific physical process is available, only a brief description of the principal characteristics of the scheme is given. This paper for most of the processes included in the model. The **Surface-Atmosphere Interaction** module is newly developed and, hence, will be documented in detail.

Convection

The model simulates dry and moist convective adjustments, shallow and penetrative cumulus convections. The dry and moist adjustment processes are assumed to occur in the free

atmosphere, and to instantaneously redistribute the atmospheric properties in the vertical column while no precipitation nor cloud is produced. In contrast, both shallow and penetrative convections are assumed to originate in the planetary boundary layer (PBL), and to carry its mean properties into the free atmosphere. The shallow convection is associated with nonprecipitating low–level cumulus clouds, while the penetrative convection produces both precipitation and deep cumulus clouds.

The lapse rate may occasionally become dry adiabatically unstable, especially in the stratosphere. When this occurs anywhere within the model atmosphere, the temperature is adjusted to restore stability under sensible heat conservation, and moisture and momentum are fully mixed between the unstable layers in a conserving manner. A moist convective adjustment process after Manabe et al. (1965) simulates midlevel convection originating above the PBL. When the lapse rate exceeds moist adiabatic from one layer to the next and saturation occurs in at least one of these layers, mass is mixed such that either the lapse rate is restored to moist adiabatic or saturation is eliminated.

Shallow (nonprecipitating) cumulus convection is parameterized by the Albrecht et al. (1986) scheme that uses an effective mass flux representation of convective heat and moisture fluxes. The effective cumulus mass flux is assumed to vary linearly with vertical σ–coordinate (decreasing upward) through the entire cloud layer and zero at the cloud top. Thus, the determination of the mass flux profile is simplified to the specification of the mass flux at the cloud base, which in turn is parameterized as a function of PBL convective velocity, surface evaporation and sensible heat flux. For shallow convection to occur, the lowest prognostic level relative humidity must be at least 90 percent and temperature above $-10°C$, the lifted condensation level is within 175 hPa of the surface, and there is moist adiabatic instability that produces a positive equivalent buoyancy force within the cloud layer. The main effect of the parameterization is to enhance the vertical moisture transport in the absence of large–scale moisture convergence. The moisture flux out of the cloud layer is generally substantial and is associated with neither precipitation nor diffusion.

Penetrative (precipitating) cumulus convection is simulated by the Arakawa and Schubert (1974) scheme, as implemented by Lord (1978) and Lord et al. (1982). The scheme predicts convective mass fluxes from mutually interacting cumulus subensembles which have different entrainment rates and levels of neutral buoyancy that define the tops of the clouds and their associated convective updrafts. A full spectrum of cumulus clouds of depths compatible with the vertical discretization is included. For each cumulus subensemble, an integral equation is formulated to include a positive–definite work function (defining the tendency of cumulus kinetic energy) and a negative–definite kernel (representing the effects of other subensembles). The predicted mass fluxes are positive–definite optimal solutions of this integral equation under the constraint that the rate of generation of conditional convective instability by the large–scale environment is balanced by the rate at which the cumulus subensembles suppress this instability via large–scale feedbacks. These mass fluxes feed back on the large–scale environment by adjustments of temperature (through latent heating and compensating subsidence), moisture (through precipitation and detrainment), and momentum (through cumulus friction). Two major modifications to the original scheme were added: (1) no convection is allowed if the lowest prognostic level relative humidity is <90 percent or temperature $<17°C$; (2) a 20 percent fraction of the cumulus condensation is assumed to be evaporated into the layers where the rain falls through (see Precipitation). As a result,

deep convection is now less frequently activated, and precipitation reaching the surface is reduced while the tropospheric moisture content is increased.

Precipitation

Precipitation is produced by the penetrative convection (see Convection) and by large-scale condensation. Large-scale precipitation forms as a result of local supersaturation under stable conditions. In this case, condensation occurs to remove local supersaturation and temperature is adjusted to account for the associated latent heat release. The amount of condensate is computed from an iterative solution of the Clausius-Clapeyron equation. This is described below.

For each model layer, if $q^0 > q^*(T^0,p)$, the excess moisture is removed and temperature is increased through the latent heat release. After the adjustment, the layer air becomes just saturated:

$$q = q^*(T,p) \text{ and } F(T) \equiv (T - T^0) + \frac{L_v}{C_p}[q^*(T,p) - q^0] = 0 , \tag{1}$$

where L_v denotes the latent heat for water phase change and C_p the specific heat capacity of dry air at constant pressure, T^0 and q^0 are initial values of air temperature and water vapor mixing ratio, and $q^*(T,p)$ is the q value of saturation at temperature T and pressure p. To obtain a rapidly convergent solution to Eq.(1), we use a generalized Newton-Raphson procedure that employs the first and second derivatives of $F(T)$:

$$\Delta T \equiv T - T^0 \approx D_1 \cdot (1 - D_1 \cdot D_2) , \tag{2}$$

where $D_1 \equiv -\frac{F(T^0)}{F'(T^0)}$ and $D_2 \equiv \frac{F''(T^0)}{2F'(T^0)}$ are respectively the first and second order Newton-Raphson corrections, and $F'(T) = 1 + \frac{L_v}{C_p}\frac{\partial q^*(T,p)}{\partial T}$ and $F''(T) = 1 + \frac{L_v}{C_p}\frac{\partial^2 q^*(T,p)}{\partial T^2}$. Note that $q^* = \frac{\varepsilon e^*}{p - (1-\varepsilon)e^*}$ and $\frac{de^*}{dT} = -\frac{L_v}{R_v}\frac{e^*}{T^2}$, where $\varepsilon \equiv R_d / R_v$, e^* is the saturation vapor pressure, R_d and R_v the gas constants for water vapor and dry air. Using these relationships, we finally obtain

$$\begin{cases} D_1 = \dfrac{\dfrac{L_v}{C_p}}{1 + \dfrac{L_v}{C_p} Y^0}[q^0 - q^*(T^0,p)] , \\ D_2 = \dfrac{\dfrac{L_v}{C_p}}{1 + \dfrac{L_v}{C_p} Y^0} \cdot \dfrac{1}{(T^0)^2}\left\{\dfrac{L_v}{R_v}\left[\dfrac{1}{2} + \dfrac{1-\varepsilon}{\varepsilon} q^*(T^0,p)\right] - T^0\right\} , \\ Y^0 = \dfrac{L_v}{R_v} \cdot \dfrac{1}{(T^0)^2} q^*(T^0,p) \cdot \left[1 + \dfrac{1-\varepsilon}{\varepsilon} q^*(T^0,p)\right] . \end{cases} \tag{3}$$

Note that the algorithm converges so rapidly that no iteration is required for removing supersaturation likely to be encountered in a GCM. The necessary condition for convergence of the algorithm is $F(T) \cdot [F'(T) \cdot \Delta T] \leq 0$ or $D_1 \cdot D_2 \leq 1$. Occasionally this condition may

be invalid, especially in model top layers. When this happens, the extremely excessive moisture is first removed as liquid water (precipitated off) without latent heat release so that the relative humidity is reduced to meet the condition. Finally, the condensation rate is calculated as $C_{ss} = \frac{C_p}{L_v}\Delta T$.

Evaporation of both the large–scale and convective condensates is also modeled. For large–scale precipitation, evaporation occurs in all unsaturated layers below its origin and is parameterized by the Schlesinger and Oh (1988) scheme. Evaporating amount is proportional to the saturation deficit of the layer where the rain falls through, but cannot exceed the precipitation flux at the layer top. For penetrative cumulus convection, water / ice that is detrained at the cloud top is assumed to evaporate instantaneously. The falling convective condensate also evaporates as it acts to progressively saturate lower layers. This is achieved by reducing the convective condensate to a fraction that is proportional to the total air mass and inversely to relative humidity of the grid box. The total evaporation is assumed to be 20 percent of the total condensate that is produced by convection otherwise. In both large–scale and convective cases all precipitation that penetrates the lowest prognostic layer is allowed to fall to the surface without further evaporation. This precipitation falls as snow P_s if the surface air temperature is $<0^{\circ}$C, or rain P_R otherwise.

Cloud Formation

Cloud amount is diagnostically determined from the relative humidity, vertical velocity, atmospheric stability, and convective precipitation rate, following the Slingo (1987) approach. Convective cloud, stratiform cloud, and low–level marine stratus / stratocumulus cloud associated with temperature inversions are treated. Clouds may form everywhere except in the surface layer to prevent development of excessive low cloudiness.

The shallow and penetrative convection parameterizations (see **Convection**) determine the vertical extent of convective cloud. The shallow convection produces a single layer cloud immediately above the PBL where the convection originates. The cloud amount increases linearly with the convective moisture flux at the cloud base. For the penetrative convection, cloud is treated as a single tower in each grid box, which extends from the lifted condensation level (usually in the PBL) to the highest cloud–top level predicted by the convective scheme. In each vertical column, the total cloud amount ($\leqslant 0.8$) increases log–linearly with the convective precipitation rate. A 25 percent of the predicted amount is allowed to occupy the full depth of the convection and is distributed uniformly in the vertical, while the remaining 75 percent is treated as low–level shallow cloud filling the bottom convective layer. If the convective cloud penetrates above 400 hPa and covers more than 0.4 fractional grid area, anvil cirrus cloud associated with the outflow from the deep convection also forms and fills the top convective layer. For subsequent diagnosis of nonconvective cloud (see below), the layer relative humidity is reduced proportionally to the fraction of convective cloud present. This essentially allows for the dry sub–grid scale downdrafts in the 'environment' in which stratiform cloud is free to form.

Stratiform clouds are mainly associated with tropical disturbances and extratropical fronts. They form only when the relative humidity exceeds 80 percent, and the amount is determined as a quadratic function of this humidity excess. These clouds are modeled in high (above 400 hPa), middle (between 400 and 800 hPa), and low (below 800 hPa) domains. Within each domain, the cloud top is chosen as the layer with the maximum relative humidity, and

the cloud is only one layer thick. The amount of low and middle cloud is reduced in dry convective downdrafts by using the reduced relative humidity (see above). Low cloud is absent in regions of large–scale subsidence, and its amount increases with the vertical velocity of upward motion.

Low–level marine stratus / stratocumulus cloud forms when the lowest prognostic level relative humidity exceeds 60 percent, and is capped by strong static stability in the layer immediately above (i.e., a temperature inversion is present). In this case, the amount of low cloud increases with the strength of the inversion and the relative humidity excess.

Radiation

Both solar and terrestrial radiation schemes are adopted from NCAR CCM1 (Kiehl et al., 1987), except for cloud emissivity and surface albedo / emissivity (see below). The original codes are largely modified for computational efficiency. A brief description of the schemes follows.

Solar radiation is treated in two spectral bands: ultraviolet / visible (0.0 to 0.9 micron) and near–infrared (0.9 to 4.0 microns). Rayleigh (molecular) scattering and gaseous absorption by ozone, oxygen, carbon dioxide, and water vapor are included. Ozone absorption in the ultraviolet and visible spectral regions is obtained from the Lacis and Hansen (1974) expression. Oxygen absorption is treated as in Kiehl and Yamanouchi (1985), and near–infrared absorption by carbon dioxide is after Sasmori et al. (1972). For water vapor, the direct–beam absorption is after the Kratz and Cess (1985) method, while the reflected–beam absorption follows Lacis and Hansen (1974). In the near–infrared spectral region, water–vapor absorption by the cloud is accounted for by enhancing the path length. Cloud multiple reflection and scattering effects are also considered, where cloud albedo depends on height and solar zenith angle. Surface albedo varies with solar zenith angle, spectral band, and surface characteristics, such as snow amount, sea ice temperature, vegetation, soil moisture and color (see Section 4).

Terrestrial radiation is simulated in 5 spectral bands, with wavenumber boundaries at 0, 5, 8, 10, 12, and 22 ($10^4 m^{-1}$). The approach solving the transfer equations is to employ absorptivities and emissivities by a broad–band technique. Absorption / emission by water vapor (Ramanathan and Downey, 1986), carbon dioxide (Kiehl and Briegleb, 1991), and ozone (Ramanathan and Dickinson, 1979) is included. The overlap treatment between water vapor and other gases is described in Ramanathan and Downey (1986). Clouds are treated as graybodies: the emissivity depends on a prescribed diffusivity factor and an optical depth which is defined by cloud temperature and pressure thickness after Harshvardhan et al. (1989). [Note that the cloud emissivity in the original CCM1 version is a function of diagnostic liquid water content (Ramanathan et al., 1983).] Surface emissivity is prescribed as a function of soil color and vegetation type (see Section 4).

In both solar and terrestrial radiation calculations, partial cloud layers are treated as randomly overlapped in the vertical. For each grid column, upward / downward fluxes are computed for clear–sky and overcast conditions, and final fluxes are determined from a linear combination of these extreme cases weighted by the actual partial cloudiness in each vertical layer. The layer differential of these fluxes defines the heating rate that directly modifies air temperature, and the fluxes at the surface affect the energy balance that determines surface temperature. Note that the radiation schemes are coded such that a sequence of partial and full calculations can be done. Transmissivity and emissivity are calculated in the full radiation steps. At each intermediate partial step, the transmissivity is scaled by the instantaneous

incoming solar radiation to represent correctly the diurnal cycle, and the emissivity is scaled by the instantaneous Planck function to incorporate temperature variations.

Eddy Diffusion

Second-order vertical eddy diffusion of momentum, moisture, and heat operates above the surface, using the Boer et al. (1984) scheme. The vertically varying diffusion coefficient depends on stability (bulk Richardson number) and the vertical shear of the wind, following standard mixing-length theory. In the PBL, the coefficient is also a function of surface roughness length. The diffusion coefficient for moisture is taken to be the same as that for heat.

Note that the parameterized surface heat and moisture fluxes (see **Surface-Atmosphere Interaction**) are completely transported upward into the free atmosphere layers by two processes: shallow convection and eddy diffusion. To this regard, it is assumed that these fluxes are first transported by shallow convection (see **Convection**), and the residuals are done through the vertical eddy diffusion.

Gravity-wave Drag

The subgrid-scale momentum transport associated with gravity-wave drag is parameterized by the Palmer et al. (1986) scheme. The drag is given by the vertical divergence of the stress due to gravity waves that are excited by stably stratified flow over irregular terrain. The stress is proportional to a product of the local air density, wind and Brunt-Vaisalla frequency as well as the displacement amplitude. At the surface, this amplitude is specified in terms of the mesoscale orographic variance σ_G^2 (see Section 4). In the free atmosphere, the amplitude is derived from linear theory and dimensional considerations. As a result, the vertical structure of the amplitude is determined from a local wave Richardson number, which describes the onset of turbulent due to convective instability and the turbulent breakdown approaching a critical level. If the minimum Richardson number falls below 0.25, the gravity wave is assumed to break. Above this critical level, the wave is maintained at marginal stability, and a corresponding saturation amplitude is used to define the stress.

Surface-Atmosphere Interaction

The surface-atmosphere interaction determines the energy (radiation, sensible and latent heat), mass (precipitation and evaporation) and momentum (surface friction) exchanges between the earth's surface and the free atmosphere. It provides a comprehensive representation of the PBL and surface processes involving vegetation, snow, ice, land soil and oceans. These processes are vital to the climate and yet complex to simulate. Here, an interaction module is developed in concern of the use for a course vertical resolution GCM. This module consists of a two-layer soil model, a surface energy balance model, and a primitive plant canopy model coupled with a PBL model.

The bulk surface energy budget equation is written as

$$\begin{cases} S_n + R_a - R_0 - \rho_a L_v E_0 - \rho_a C_p Q_0 = G \ , \\ R_0 \equiv \varepsilon_s \sigma_s T_0^4 \ , \quad \rho_a = \dfrac{p_s}{R_d T_a} \end{cases} \tag{4}$$

where S_n is the net solar radiation absorbed by the surface, and R_a the atmospheric terrestrial radiation emitted down to the surface; they depend weakly on surface temperature T_0

and are provided from the radiation calculation. Parameters $\varepsilon_s, \sigma_s, L_v, C_p$ denote for surface emissivity, the Stefan–Boltzmann constant, the latent heat for water phase change and the specific heat capacity of dry air at constant pressure; they are considered to be constant or instantaneously independent of T_0. p_s is the surface pressure, ρ_a the near–surface air density, T_a the near–surface air temperature, E_0 the surface evaporation rate, Q_0 the surface sensible heating rate, and G the heat flux into the ground.

The G is implicitly derived from the two–layer soil model using an extended force–restore method (Jacobsen and Heise, 1982):

$$\begin{cases} \dfrac{\partial \theta_s}{\partial t} = -a_s \theta_s + b_s \theta_m + c_s G \\ \dfrac{\partial \theta_m}{\partial t} = -a_m \theta_m + b_m \theta_s \\ \theta_s \equiv \theta_0 - \theta_r \equiv \Theta(p_s)(T_0 - T_r) \ , \end{cases} \tag{5}$$

where $\Theta(p) \equiv (1000/p)^{\kappa}$ is the conversion coefficient from temperature to potential temperature, and $\kappa \equiv R_d / C_p$. T_r is the reference temperature representative of the deep soil boundary (see Section 4). Other parameters are defined as

$$\begin{cases} a_s = \omega_1 (1 + x + x^2) \ , \quad x \equiv \sqrt{\dfrac{\omega_2}{\omega_1}} \\ b_s = \omega_1 x \sqrt{1 + x^2} \exp\left(\dfrac{x}{1+x}\right) \\ c_s = \dfrac{2}{\eta}\left(\dfrac{1}{d_1} + \dfrac{1}{d_2}\right) \ , \quad d_i = \sqrt{\dfrac{2\lambda}{\eta \omega_i}} \\ a_m = \omega_1 x \ , \quad b_m = \omega_1 x \sqrt{1 + x^2} \exp\left(-\dfrac{x}{1+x}\right) \ , \end{cases} \tag{6}$$

where ω_1, ω_2 are the two representative frequencies of under–ground temperature waves to be resolved. Currently, they are chosen to reproduce exactly the diurnal and annual temperature waves such that $\omega_1 = 2\pi(1 \text{ day})^{-1}$ and $\omega_2 = 2\pi(365 \text{ day})^{-1}$. The backward implicit differencing solution to Eq.(5) is

$$\begin{cases} G = A_G + B_G(\theta_0 - \theta_0^0) \\ \theta_m = \dfrac{1}{1 + \omega x}(\theta_m^0 + b_m \delta t \theta_s^0) \\ B_G \equiv \dfrac{1}{c_s} \dfrac{\omega^2 x^2 + \omega(1+x)^2 + 1}{(1 + \omega x)\delta t} \ , \quad \omega \equiv \omega_1 \delta t \\ A_G \equiv \dfrac{1}{c_s}\left[\dfrac{\omega^2 x^2 + \omega(1 + x + x^2)}{(1 + \omega x)\delta t}\theta_s^0 - \dfrac{b_s}{1 + \omega x}\theta_m^0\right] \ , \end{cases} \tag{7}$$

where F^0 is the initial F value, and δt the integration time interval.

The soil volumetric heat capacity η (J / m^{3}K) and thermal conductivity λ (W / mK) are specified following McCumber and Pielke (1981):

$$\begin{cases} \lambda = \max[0.172, 418.7\exp(-P_f - 2.7)] \\ P_f = \log_{10}[\Psi_s \left(\dfrac{v_s}{v}\right)^b] \\ \eta = (1 - v)\eta_{\text{soil}} + v\eta_{\text{water}} \ , \end{cases} \tag{8}$$

where $\eta_{soil} = 1.549 \times 10^6$ is for dry soil and $\eta_{water} = 4.186 \times 10^6$ for pure water. The volumetric water content v is predicted in a framework that includes two layers of soil hydrology (Mahrt and Pan, 1984) and one layer of vegetation canopy (Pan and Mahrt, 1987). The soil water transport equation can be written as

$$\frac{\partial v}{\partial t} = \frac{\partial}{\partial z}\left(D\frac{\partial v}{\partial z}\right) + \frac{\partial K}{\partial z} + E_z \quad . \tag{9}$$

Here, the hydraulic conductivity K and diffusivity D are functions of v as specified in Clapp and Hornberger (1978):

$$K = K_s\left(\frac{v_s}{v}\right)^{2b+3} \quad , \quad D = \frac{bK_s\Psi_s}{v_s}\left(\frac{v_s}{v}\right)^{b+2} \tag{10}$$

where the soil physical parameters b, v_s, Ψ_s and K_s depend on soil texture (see Section 4).

In a two-layer soil domain, the integration of Eq.(9) over the upper layer of depth z_1 and the lower layer of depth $z_2 - z_1$ leads to

$$\begin{cases} (z_1)\dfrac{\partial v_1}{\partial t} = -\left[D(v)\dfrac{\partial v}{\partial z} + K(v)\right]_{-z_1} + I - (E_1 - E_2) \\ (z_2 - z_1)\dfrac{\partial v_2}{\partial t} = +\left[D(v)\dfrac{\partial v}{\partial z} + K(v)\right]_{-z_1} - K(v)_{-z_2} - E_2 \\ v_1 = \dfrac{1}{(z_1)}\displaystyle\int_{-z_1}^{0} v dz \quad , \quad v_2 = \frac{1}{(z_2 - z_1)}\int_{-z_2}^{-z_1} v dz \quad , \end{cases} \tag{11}$$

where E_1 is the direct evaporation of soil water to the atmosphere, E_2 the transpiration originating from the deeper vegetation root zone, I the infiltration rate. Currently, z_1, z_2 are set to 5 and 100 cm. Let $\frac{\partial v}{\partial t} \approx \frac{v - v^0}{\delta t}$, $K(v)_{-z_2} \approx 0$ and $\left[D(v)\frac{\partial v}{\partial t}\right]_{-z_1} \approx D(v_1^0)\frac{1}{2}\left(\frac{v_1 - v_2}{z_2/2} + \frac{v_1^0 - v_2^0}{z_2/2}\right)$ the implicit differencing solution to Eq.(11) is

$$\begin{cases} a_1 v_1 + b_1 v_2 = c_1 \\ a_2 v_1 + b_2 v_2 = c_2 \\ a_1 = +1 - b_1, \quad b_1 \equiv -\dfrac{\delta t}{z_1 z_2} D(v_1^0) \\ a_2 = -1 - b_2, \quad b_2 \equiv -\left[1 + \dfrac{\delta t}{(z_2 - z_1)z_2} D(v_1^0)\right] \\ c_1 \equiv \dfrac{\delta t}{z_1}[I - (E_1 - E_2) - K(v_1) - D(v_1)\dfrac{v_1 - v_2}{z_2}]^0 + v_1^0 \\ c_2 \equiv \dfrac{\delta t}{z_2 - z_1}[E_2 - K(v_1) - D(v_1)\dfrac{v_1 - v_2}{z_2}]^0 - v_2^0 \quad . \end{cases} \tag{12}$$

The explicit solution to the above equation is

$$\begin{cases} v_1 = \Delta^{-1}(c_2 b_1 - c_1 b_2) \\ v_2 = \Delta^{-1}(c_1 a_2 - c_2 a_1) \\ \Delta \equiv a_2 b_1 - a_1 b_2 = -(b_1 + b_2) \quad . \end{cases} \tag{13}$$

The direct soil evaporation is most appropriately associated with the soil moisture of an upper thin layer while water for transpiration originates more from the deeper root zone. Thus, the following formulations can be used:

$$\begin{cases} I = \min(P_R, I_{\max}), \quad I_{\max} = \dfrac{2}{z_1} D(v_s)(v_s - v_1) + K(v_s) \\ E_1 = E_0 - E_S - \sigma_f E_C \ , \quad E_2 = \dfrac{g_2}{g_1 + g_2} \sigma_f E_T \\ E_S = (1 - \sigma_f) E_{TB} + \sigma_f (E_T + E_C) \\ g_1 = \dfrac{z_1}{z_2} g(v_1) \ , \quad g_2 = \dfrac{z_2 - z_1}{z_2} g(v_2) \\ g(v) \equiv \max\left[0, \min\left(1, \dfrac{v - v_c}{v_r - v_c}\right)\right] . \end{cases} \tag{14}$$

Note that any rainfall P_R which cannot infiltrate or re–evaporate is specified as runoff. The vegetation shading factor σ_f depends on vegetation type and the time of the year, which is now interpolated from the prescribed summer and winter values (see Section 4). In the $g(v)$ formulation, it is assumed that at v_r the soil moisture deficit begins to reduce the vegetation root uptake and transpiration which ceases at v_c Following Wetzel and Change (1987) and Clapp and Hornberger (1978), we have

$$v_r = 0.75 v_s \ , \quad v_c = v_s \left(\frac{\Psi_s}{\Psi_c}\right)^{\frac{1}{b}} \tag{15}$$

where Ψ_c is prescribed as 200 m.

The E_{TB} is the maximum sustainable or threshold evaporation rate of bare soil and is parameterized as Dickinson (1984):

$$\begin{cases} E_{TB} = F_K \dfrac{1.02 D_{\max}}{\sqrt{z_1 z_2}} \left(\dfrac{v_1}{v_s}\right)^{3 + b_f} \left(\dfrac{\bar{v}}{v_s}\right)^{b - b_f} \\ F_K = \left(1 + 1550 \dfrac{10^{-9}}{D_{\max}}\right) \dfrac{b - 3.7 + 5/b}{b + 5} \\ b_f = 5.5 - 0.8b[1 + 0.1(b - 4)\log_{10}(K_s / K_r)] \\ \bar{v} = \dfrac{(z_2 - z_1) v_2 + z_1 v_1}{z_2} \ , \quad D_{\max} = \dfrac{b \Psi_s K_s}{\rho_{wm}} \end{cases} \tag{16}$$

where K_r is the reference hydraulic conductivity, and ρ_{wm} the fraction of saturated soil filled by water; they are prescribed as 0.01 mm / s and 0.5 respectively.

The E_T is the total transpiration from the vegetation root zone, and E_c the evaporation of the precipitation intercepted by the canopy; they are determined as Noilhan and Planton (1989):

$$\begin{cases} E_C = \sqrt{\dfrac{C_W}{C_{WC}}}\,E_P \ , \quad E_T = \left(1-\sqrt{\dfrac{C_W}{C_{WC}}}\right)E_P\dfrac{r_a}{r_a+r_c} \\ r_a^{-1} = C_Q \ , \quad r_c^{-1} = \max(r_{c\max}^{-1}, r_{c\min}^{-1}A_c F_1^{-1}F_2F_3F_4^4 \\ F_1 = \dfrac{1+f_1}{f_1+r_{c\min}/r_{c\max}} \ , \quad f_1 = 0.55\dfrac{S_I}{S_{PS}}\dfrac{2}{A_c} \\ F_2 = g_1+g_2 \ , \quad F_4 = 1-0.0016(298-T_a)^2 \\ F_3 = 1-0.25[e^*(T_0)-e_a] \ , \quad e_a = \dfrac{p_s q_a}{\varepsilon+(1-\varepsilon)q_a} \end{cases} \tag{17}$$

where q_a is the near-surface air water vapor mixing ratio, S_I the solar radiation incident on the surface. S_{PS} is the limit of photosynthetically active radiation; $r_{c\min}$ and $r_{c\max}$ are the minimum and maximum surface resistances; A_c is the projected area of green leaf per unit surface area; they are prescribed as functions of vegetation type (see Section 4). C_Q is the bulk surface turbulent transfer coefficient for moisture.

The C_W, C_{WC} are the canopy water content and capacity. They are determined following Dickinson (1984):

$$\begin{cases} \dfrac{\partial C_W}{\partial t} = \sigma_f(P_R - E_C) \\ C_{WC} = 0.2\sigma_{f\max}A_{c\max} \ , \end{cases} \tag{18}$$

where $\sigma_{f\max}$, $A_{c\max}$ are maximum (or summertime) values of σ_f and A_c.

Considering the atmospheric moisture demand of the lowest prognostic layer and the availability of soil moisture / snow for evaporation / sublimation, the potential surface evaporation E_p and the actual surface evaporation E_0 can be determined by

$$\begin{cases} E_p = C_Q[q^*(T_0,p_s)-q_a] \\ E_0 = \min(\beta_E E_p, E) \quad \text{if} \quad E_p > 00, \quad \text{else} = E_p \\ E = (1-\delta_S)E_S + \delta_S\dfrac{M_S}{\delta t} \ , \quad \delta_S = \min\left(1, \sqrt{\dfrac{M_S}{M_{Sr}}}\right) \\ \beta_E = \delta_S + (1-\delta_S)\min\left(0.25, \dfrac{1}{3}\dfrac{v}{v_s}\right) \end{cases} \tag{19}$$

where M_S is the predicted snow mass (see below), and M_{Sr} is the corresponding reference value for the snow to cover the entire grid and is prescribed as 10 kg / m^2.

Eq.(4) can be solved using a backward implicit differencing scheme such that

$$\begin{cases} F_N^0 - \beta_G(\theta_0 - \theta_0^0) - \rho_a C_p Q_0 = 0 \\ F_N^0 \equiv [S_n + R_a - R_0 - \rho_a L_v E_0 - A_G]^0 \\ \beta_G \equiv B_G + E_G + R_G \ , \end{cases} \tag{20}$$

where E_G, R_G are factors accounting for the T_0-dependence of E_0 and R_0. They are derived using the following approximations:

$$\begin{cases} R_0(T_0) \approx R_0(T_0^0) + R_G(\theta_0 - \theta_0^0) \\ R_G \equiv \dfrac{\partial R_0}{\partial T_0}\Theta(p_s) = 4\varepsilon_s \sigma_s (T_0^0)^3 \Theta(p_s) \\ \rho_a L_v E_0(T_0) \approx \rho_a L_v E_0(T_0^0) + E_G(\theta_0 - \theta_0^0) \\ E_G \equiv \rho_a L_v \dfrac{\partial E_0}{\partial T_0}\Theta(p_s) = \rho_a L_v \beta'_E C_Q \left[\dfrac{\partial q^*(T_0, p_s)}{\partial T_0}\right]^0 \Theta(p_s) \end{cases} \quad (21)$$

Note that E_G is non-zero only if E_0 is a function of E_p. Thus,

$$\beta'_E = \begin{cases} 1 & \text{if } E_p \leqslant 0 \\ \beta_E & \text{if } E > \beta_E E_p > 0 \\ 0 & \text{otherwise} \end{cases} \quad (22)$$

The determination of Q_0 follows the Delage (1986) approach, which considers three distinct periods: the night, morning and afternoon phases. During the night phase, $F_N^0 \leqslant 0$ and $\theta_0^0 < \theta_L$. Here $\theta_L = T_L \Theta(p_L)$ is the potential temperature at the lowest prognostic level, and T_L, p_L are the corresponding air temperature and pressure. In this case, the nocturnal boundary layer top height h is predicted as Nieuwstadt and Tennekes (1981):

$$\begin{cases} \dfrac{\partial h}{\partial t} = \dfrac{h_e - h}{\tau} \\ \tau = \dfrac{3.5}{|f|}, \quad h_e = h_{ec} + f_{ef}\sqrt{\dfrac{L_{mo} C_M}{|f|}} \end{cases} \quad (23)$$

where h_{ec}, f_{ef} are currently prescribed as 435 m and 0.7. $|f|$ is the absolute value of the Coriolis parameter, L_{mo} the Monin-Obukhov length, and C_M the bulk surface turbulent transfer coefficient for momentum. The implicit differencing solutions of Eqs.(20) and (23) become

$$\begin{cases} \theta_0 = \theta_L + \dfrac{3f_h}{h} Q_n, \quad Q_n \equiv \displaystyle\int_{t_n}^{t} Q_0 dt \\ h = \left(1 + \dfrac{\delta t}{2\pi}\right)^{-1}\left[h^0 - \dfrac{\delta t}{2\pi}(2h_e^0 - h^0)\right] \\ Q_n - Q_n^0 = \dfrac{\delta t}{\rho_a C_p}[F_N^0 - \beta_G(\theta_0 - \theta_0^0)] \\ f_h = \sqrt{\dfrac{8z_L}{9h}} \quad \text{if } z_L < \dfrac{h}{2}, \quad \text{else} = 1 - \dfrac{h}{6z_L} \end{cases} \quad (24)$$

where t_n is the time t at the beginning of the night, and z_L the height of the lowest prognostic level above local resolved terrain $\bar{z}_s$. A simple manipulation of Eq.(24) leads to an explicit solution:

$$Q_n = \left(1 + \frac{3f_h \beta_G \delta t}{\rho_a C_p}\right)^{-1}\left\{Q_n^0 + \frac{\delta t}{\rho_a C_p}[F_N^0 + \beta_G(\theta_0^0 - \theta_L)]\right\}. \quad (25)$$

During the morning phase, $F_N^0 > 0$ and $\theta_0^0 < \theta_L$. In this case, the boundary layer height is assumed to increase from the beginning of the morning (at time t_m) as a quadratic function of the potential temperature increase. This results in

$$\begin{cases} \theta_0 = \theta_0' + \theta_L - \theta_{Lj} - \dfrac{Q_m^0}{2z_L} \\ \theta_0' = \theta_{0j} + \sqrt[3]{\dfrac{3(\theta_{Lj}-\theta_{0j})^2}{f_{hj}^2 h_j} Q_m} \quad , \quad Q_m \equiv \int_{t_m}^{t} Q_0 \, dt \\ Q_m - Q_m^0 = \dfrac{\delta t}{\rho_a C_p}[F_N^0 - \beta_G(\theta_0 - \theta_0^0)] \\ h = h_j \left(\dfrac{\theta_0' - \theta_{0j}}{\theta_h - \theta_{0j}} \right)^2 \quad \text{is pre-assumed} \ , \end{cases} \tag{26}$$

where F_j is the F value at time t_m. Eq.(26) can be easily transferred to a cubic equation of θ_0, which has the following solution:

$$\begin{cases} \theta_0 = a_3 + \sqrt[3]{x+y} - \sqrt[3]{x-y} \\ x = \sqrt{y^2 + \left(\dfrac{b_3 c_3}{3}\right)^3} \quad , \quad y = \dfrac{b_3}{2}(d_3 - a_3 c_3) \\ a_3 \equiv \theta_L - \theta_{Lj} + \theta_{0j} - \dfrac{Q_m^0}{2z_L} \quad , \quad b_3 \equiv \dfrac{3}{f_{hj}^2 h_j}(\theta_{Lj} - \theta_{0j})^2 \\ c_3 \equiv \dfrac{\beta_G \delta t}{\rho_a C_p} \quad , \quad d_3 \equiv Q_m^0 + \dfrac{\delta t}{\rho_a C_p}(F_N^0 + \beta_G \theta_0^0) \ . \end{cases} \tag{27}$$

During the afternoon phase, $\theta_0^0 \geqslant \theta_L$. In this case, Q_0 is directly parameterized by the bulk aerodynamic method and, thus, the solution of Eq.(20) is given by

$$\begin{cases} Q_0 = C_H(\theta_0 - \theta_L) \\ \theta_0 = \dfrac{F_H^0 + \beta_G \theta_0^0 + \rho_a C_p C_H \theta_L}{\beta_G + \rho_a C_p C_H} \ , \end{cases} \tag{28}$$

where C_H is the bulk surface turbulent transfer coefficient for heat.

The snow mass M_S is predicted by

$$\begin{cases} \dfrac{\partial M_S}{\partial t} = P_S - E_S^* - S_m \\ E_S^* = \min\left[\dfrac{\delta_S}{\beta_E} \dfrac{\rho_a L_v E_0}{L_v + L_f} \ , \ \dfrac{M_S^0}{\delta t} + P_S \right] , \end{cases} \tag{29}$$

where L_f is the latent heat of fusion, P_S the snowfall rate, E_S^* the snow evaporation or sublimation rate. The snowmelt rate S_m depends on how much surface heating is available. On the basis of Eqs.(22), (26–27) and (28), this heating can be estimated by

$$\begin{cases} H(\theta) = F_N^0 - \beta_G(\theta - \theta_0) - \dfrac{\rho_a C_p}{\delta t}(Q'_n - Q_n) & \text{for night} \\ H(\theta) = F_N^0 - \beta_G(\theta - \theta_0) - \dfrac{\rho_a C_p}{\delta t}(Q'_m - Q_m) & \text{for morning} \\ H(\theta) = F_N^0 - \beta_G(\theta - \theta_0) - \rho_a C_p C_H(\theta - \theta_L) & \text{for afternoon} \\ Q'_n \equiv \dfrac{h(\theta - \theta_L)}{3f_h} \ , \ Q'_m \equiv \dfrac{(\theta - a_3)^3}{b_3} \ \text{if } b_3 \neq 0 \ , \ \text{else} \equiv 2z_L(\theta_L - \theta) \ . \end{cases} \tag{30}$$

If $H(\theta) > 0$, the surface temperature can rise until it reaches the melting point T_{ice}, whereupon snowmelt begins. Thus, provided $\theta = \theta_{ice} \equiv T_{ice}\Theta(p_s)$, the snowmelt rate is given by

$$S_m = \min[H(\theta_{ice}) / L_f, M_s^0 / \delta t + P_S] \ . \tag{31}$$

The bulk surface turbulent transfer coefficients for moisture C_Q, heat C_H and momentum C_M depend on the PBL stability parameter L_{mo} and the local surface roughness length. Currently, it is assumed that $C_H = C_Q$. In addition, we use the following notations:

$$C_M \equiv C_m w_* \ , \quad C_Q \equiv C_q w_* \ , \quad w_* \equiv C_m w_a \tag{32}$$

where w_a is the magnitude of near-surface wind.

For the neutral condition, $\delta\theta_{L0} \equiv \theta_L - \theta_0 = 0$, we have

$$L_{mo} = 0 \ , \quad C_m = \frac{k_c}{\ln(z_L / z_0)} \ , \quad C_q = \frac{k_c}{\ln(z_L / z_q)} \tag{33}$$

where $k_c = 0.4$ is the Karman constant (Hoestroem, 1985), and z_0, z_q are the roughness lengths for momentum and for moisture / heat (see Section 4).

For the unstable condition, $\delta\theta_{L0} < 0$, we use the Dyer and Bradley (1982) scheme:

$$\begin{cases} L_{mo} = \dfrac{\overline{T}_*}{k_c g} \dfrac{w_*^2}{C_q \delta\theta_{L0}} \ , \ \overline{T}_* \approx T_L(1 + 1.7 \times 10^{-6} T_L q_L) \\ C_m = k_c \left\{ \ln\left(\dfrac{z_L}{z_0}\right) + \ln\left[\dfrac{(\xi_0^2 + 1)(\xi_0 + 1)^2}{(\xi_0^2 + 1)(\xi + 1)^2}\right] + 2(\tan^{-1}\xi - \tan^{-1}\xi_0) \right\}^{-1} \\ C_q = k_c \left[\ln\left(\dfrac{z_L}{z_q}\right) + \ln\left(\dfrac{\zeta_0 + 1}{\zeta + 1}\right)^2 \right]^{-1} \\ \xi(z) \equiv \sqrt[4]{1 - 28\dfrac{z}{L_{mo}}} \ , \quad \zeta(z) \equiv \sqrt{1 - 14\dfrac{z}{L_{mo}}} \\ \xi = \xi(z_L) \ , \quad \xi_0 = \xi(z_0) \ , \quad \zeta = \zeta(z_L) \ , \quad \zeta_0 = \zeta(z_q) \end{cases} \tag{34}$$

where g is the gravitational acceleration, and $\overline{T}_*$ the averaged virtual temperature (Large and Pond, 1982). Because L_{mo}, C_m, C_q depend on each other, multiple iterations are needed to obtain the final values. L_{mo} is initially set to -36 m and, in general, a steady solution can be reached after 3 iterations.

For the stable condition, $\delta\theta_{L0} > 0$, we use a corrected Miyakoda and Sirutis (1986) scheme:

$$\begin{cases} C_m = k_c[\varphi(\chi_L) - \varphi(\chi_0)]^{-1} \ , \quad C_q = k_c[\varphi(\chi_L) - \varphi(\chi_q)]^{-1} \\ \varphi(\chi) = \begin{cases} \ln\chi + 5\chi & \text{if} \quad 0 < \chi \leqslant 0.5 \\ 8\ln\chi + 4.25\chi^{-1} - 0.5\chi^{-2} + 0.852 & \text{if} \quad 0.5 < \chi \leqslant 6 \\ 0.76\chi + 11.32 & \text{if} \quad \chi > 6 \end{cases} \\ \chi_L = z_L / L_{mo} \ , \quad \chi_0 = z_0 / L_{mo} \ , \quad \chi_q = z_q / L_{mo} \\ L_{mo} = z_L / R_i \ , \quad R_i = g z_L \delta\theta_{L0} / \overline{T}_* w_L^2 \end{cases} \tag{35}$$

where w_L is the magnitude of the lowest prognostic level wind, R_i the bulk Richardson number in the PBL, and $\overline{T}_*$ as in Eq.(34). Note that corrections are made in Eq.(35) to remove erroneous discontinuities in the original scheme.

The near-surface air temperature and water vapor mixing ratio are estimated using the Arakawa (1972) approach. It is assumed that the surface layer is in equilibrium so that the

sensible and latent heat fluxes from the ground equal those into the lowest prognostic layer. This results in

$$\begin{cases} q_a = \dfrac{C_Q \beta_E q^*(T_0^0, p_s) + D_{az} q_L}{(C_Q \beta_E + D_{az})} \\ T_a = \dfrac{C_Q T_0^0 + D_{az}[\theta_L \Theta(p_s) - T_b]}{(C_Q + D_{az})} \\ T_b \equiv \dfrac{g z_L}{R_d (1+\gamma_a)} \dfrac{q_a}{q^*(T'_a, p_s)} \left[\kappa \gamma_a - \dfrac{L_v}{C_p} \dfrac{q^*(T'_a, p_s)}{T'_a} \right] \\ T'_a = T_L + \dfrac{g}{C_p} z_L \ , \quad \gamma_a \equiv \dfrac{L_v}{C_p} \dfrac{\partial q^*}{\partial T}(T'_a, p_s) \ , \quad D_{az} \equiv \dfrac{D_a}{z_L} \end{cases} \tag{36}$$

where D_a is the PBL eddy diffusion coefficient and is parameterized as Deardoff (1967):

$$D_a = \begin{cases} D_{an} \dfrac{1 - 1.927 \times 10^3 \delta\theta_{L0} / z_L}{1 - 1.752 \times 10^4 \delta\theta_{L0} / z_L} & \text{if} \quad \delta\theta_{L0} < 0 \\ D_{an} & \text{if} \quad \delta\theta_{L0} = 0 \\ D_{an} \dfrac{1}{1 + 50 R_i} & \text{if} \quad \delta\theta_{L0} > 0 \end{cases} \tag{37}$$

where R_i is defined as in Eq.(35), and D_{an} is prescribed as 60 m^2/s.

The near–surface wind is estimated as Bourke (1974):

$$\begin{cases} u_a = u_L \cos\alpha_c + v_L \sin\alpha_c \sin\varphi \\ v_a = v_L \cos\alpha_c - u_L \sin\alpha_c \sin\varphi \ , \end{cases} \tag{38}$$

where φ is the grid latitude, u_L, v_L are the eastward and southward components of the lowest prognostic level wind. The crossisobar angle α_c can be specified as Hansen et al. (1983):

$$\sin\alpha_c = C_M / \sqrt{2|f| D_a} \quad \text{if} \quad |f| \neq 0, \quad \text{else} = 0 \tag{39}$$

The wind magnitudes are then defined by

$$w_a = \max(\sqrt{u_a^2 + v_a^2}, w_G), \quad w_L = \max(\sqrt{u_L^2 + v_L^2}, w_G) \tag{40}$$

where w_G is a gustiness parameter and is prescribed as 2 m / s.

Over open water and permanent land or sea / pack ice, special considerations are taken. It is assumed that these surfaces are always saturated in water and, thus, surface water content v is not predicted. For the same reason, surface evaporation and sensible heating rates are simply defined by the bulk aerodynamic method:

$$E_0 = E_p = C_Q [q_0^* - q_a] \ , \quad Q_0 = C_H (T_0 - T_a) \tag{41}$$

where $q_0^* \equiv q^*(T_0, p_s)$. Note that q_a is now constrained by the upper bound of Bowen ratio to forbid supersaturation above an evaporating water (or sublimating ice) surface. According to Philip (1987), this upper bound is

$$B_0 \equiv \frac{\rho_a C_p Q_0}{\rho_a L_v E_0} = \frac{C_p}{L_v} \frac{C_H}{C_Q} \frac{T_0 - T_a}{q_0^* - q_a} \leqslant B_0^* \approx \frac{C_p}{L_v} \left[\frac{\partial q^*}{\partial T}(T_a, p_s) \right]^{-1} . \tag{42}$$

The above inequality can be re–formulated as

$$q_a = \min\left[q_a, q_0^* - \frac{C_H}{C_Q}(T_0 - T_a)\frac{\partial q^*}{\partial T}(T_a, p_s)\right] \quad \text{if} \quad q_0^* > q_a \ , \tag{43}$$

where q_a, T_a on the right hand side are given by Eq.(36).

The determination of bulk surface turbulent transfer coefficients over water or ice follows that over land using Eqs.(32)–(35) with two exceptions. First, surface roughness lengths differ (see Section 4). Second, for the unstable condition, the Monin–Obukhov length is now explicitly defined as Large and Pond (1982):

$$\begin{cases} L_{mo} = \overline{T}_* w_L^2 [100(T_0 - T'_b) + 1.7 \times 10^{-4} \overline{T}_*^2 (q_0^* - q'_b)]^{-1} \\ T'_b \equiv \theta_L \Theta(p_s) \ , \quad q'_b \equiv \dfrac{q_L}{q^*(T_L, p_L)} q^*(T'_b, p_s) \end{cases} \tag{44}$$

and therefore no iteration is needed to solve Eq.(34).

The water surface temperature is currently prescribed from observations (see Section 4) and, hence, the T_0 prediction is not needed for open water. The ice surface temperature is predicted by Eq.(4) using a modified G formulation:

$$G = \Gamma_1 \frac{\partial T_0}{\partial t} + \begin{cases} \dfrac{\lambda_I}{d_I}(T_0 - T_d) & \text{for sea ice} \\ \alpha_R \Gamma_1 \omega_1 (T_0 - T_r) & \text{for land ice} \end{cases} \tag{45}$$

where Γ_1 is the bulk thermal heat capacity over the e–folding depth of the diurnal temperature wave (frequency ω_1), λ_I the thermal conductivity, d_I the thickness of sea ice (prescribed as 3 m), T_d the sea–surface temperature below the ice (prescribed as 271.5 K), T_r the reference temperature representative of the deep land ice boundary (see Section 4), α_R the restoring coefficient (prescribed as 0.4). According to Priestley (1959), $\Gamma_I = 3.4702 \times 10^5$ J / m^{2}K, $\lambda_I = 2.2605$ W / mK. In Eq.(45), the second term on the right hand side accounts for the conduction heat flux at an infinitesimal distance below the surface. The backward implicit differencing solution to Eq.(4) now becomes

$$\begin{cases} T_0 = \dfrac{F_N^0 + \beta_G T_0^0 + \rho_a C_p C_H T_a}{\beta_G + \rho_a C_p C_H} \\ F_N^0 \equiv [S_n + R_a - R_0 - \rho_a L_v E_0 - A_G]^0 \\ \beta_G \equiv B_G + E_G + R_G \\ R_G \equiv 4\varepsilon_s \sigma_s (T_0^0)^3 \ , \quad E_G \equiv \rho_a L_v C_Q \left[\dfrac{\partial q^*(T_0, p_s)}{\partial T_0}\right]^0 \\ A_G = \dfrac{\lambda_I}{d_I}(T_0^0 - T_d) \quad \text{for sea ica, else} = \alpha_R \Gamma_I \omega_1 (T_0^0 - T_r) \\ B_G = \dfrac{\Gamma_I}{\delta t} + \dfrac{\lambda_I}{d_I} \quad \text{for sea ice, else} = \dfrac{\Gamma_I}{\delta t} + \alpha_R \Gamma_I \omega_1 \ . \end{cases} \tag{46}$$

Snow is allowed to accumulate over ice and is predicted by Eqs.(29)–(31). In this case, however, $\beta_E = 1$, $\delta_S = 1$ in Eq.(29), $H(T)$ is defined for afternoon in Eq.(30), and all θ values are now replaced by the corresponding T values.

An additional surface–atmosphere exchange flux used in **Eddy–Diffusion** is the momentum stress, which is determined by

$$\vec{F}_M = -\rho_a C_M \vec{V}_a = -\rho_a C_M \{u_a, v_a\} \ . \tag{47}$$

IV. SURFACE BOUNDARY CONDITIONS

The models continental outline, mean terrain elevation and mesoscale variance are determined on the basis of the 10-minute resolution data prepared by the US Navy Fleet Numerical Oceanography Center at Monterey (Joseph, 1980). In addition to distinguishing between water and land surfaces, the model further differentiates surfaces by ice, vegetation, soil texture and soil color. The vegetation types are derived from the Matthews (1983) data with $1^\circ \times 1^\circ$ resolution and 32 classifications, while the soil textures and colors are constructed from the Wilson and Henderson-Sellers (1985) data with $1^\circ \times 1^\circ$ resolution and 21-type combinations of 3-color (light, medium, dark), 3-texture (coarse, intermediate, fine) and 3-drainage (poor, impeded, free) classes. These data values are aggregated to the GCM resolution using area average and appropriate composite. The precise algorithm for specifying the GCM grid values follows.

For any specific quantity $\bar{F}$ in a GCM grid box and F_i at data cell i within the box,

$$\bar{F} = \sum_i A_i F_i / \sum_i A_i \ , \tag{48}$$

where A_i denotes the area of data cell i and the summation extends over all data cells within the GCM grid box. For the continental outline, F_i is set to 1 for land and 0 for water at each $10^\circ \times 10^\circ$ data cell and, thus, the fractional area of land $\bar{F}$ is obtained. Grid boxes with $\geqslant 50\%$ land area are taken to be land (including permanent pack ice) or water otherwise. The mean terrain elevations $\bar{z}_s$ are determined by using $10' \times 10'$ data cell topographic heights z_{si}. The terrain mesoscale variances σ_G^2 are then calculated by using $F_i \equiv (z_{si} - \bar{z}_s)^2$. A 9-point spatial smoothing is performed on both $\bar{z}_s$ and σ_G^2. In addition, σ_G^2 is limited to $(400\ \text{m})^2$ to prevent two-grid noise near steep mountains.

Table 1. Soil Physical Parameters as Functions of Soil Texture (Cosby et al., 1984)

Soil Texture	Fig. 1b Symbol	Clay Fraction	b	v_s cm^3/cm^3	Ψ_s cm	K_s 10^{-2}mm/s
Sand	1	0.03	2.79	0.339	6.92	4.66
Loamy sand	2	0.06	4.26	0.421	3.63	1.41
Sandy loam	3	0.10	4.74	0.434	14.13	0.52
Silt loam	4	0.13	5.33	0.476	75.86	0.28
Loam	5	0.18	5.25	0.439	35.48	0.34
Sandy clay loam	6	0.27	6.77	0.404	13.49	0.45
Silt clay loam	7	0.34	8.72	0.464	61.66	0.20
Clay loam	8	0.39	8.17	0.465	26.30	0.24
Sandy clay	9	0.42	10.73	0.406	9.77	0.72
Silt clay	%	0.47	10.39	0.468	32.36	0.13
Light clay	*	0.58	11.55	0.468	46.77	0.10

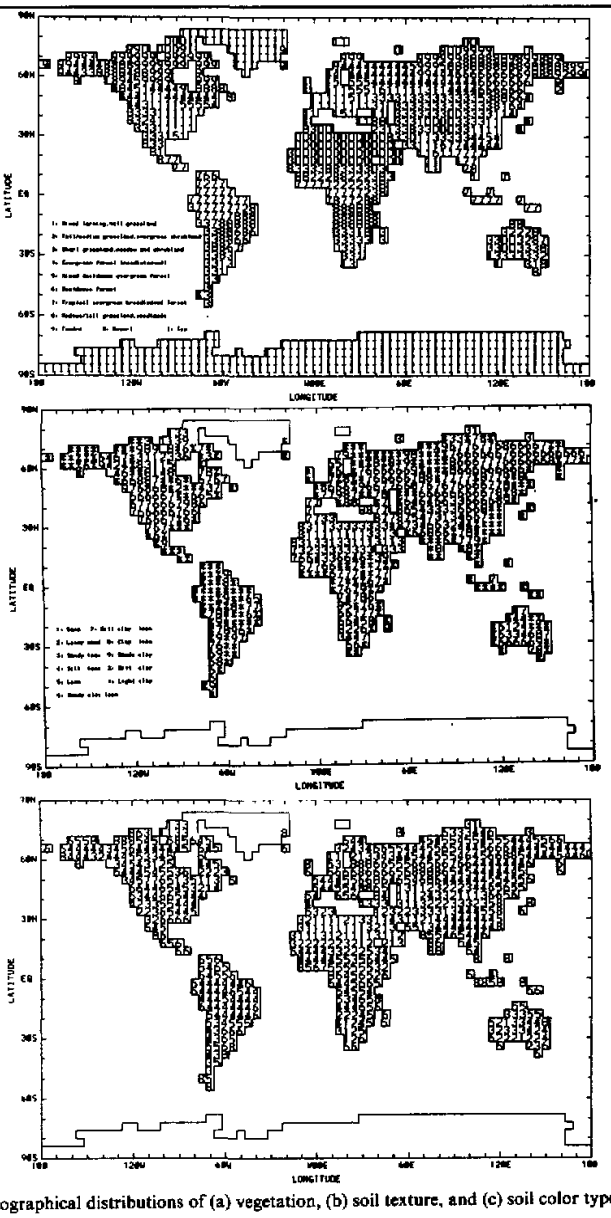

Fig. 1. Geographical distributions of (a) vegetation, (b) soil texture, and (c) soil color types on the $4° \times 5°$ GCM grid resolution. The segmentation lines form the continental outline.

Table 2. Bare Soil Surface Solar Albedo α_b and Terrestrial Emissivity ε_b as Functions of Soil Color

Soil color		Light							Dark
Fig. 1c Symbol		1	2	3	4	5	6	7	8
α_b	0.2–0.5μ	0.12	0.11	0.10	0.09	0.08	0.07	0.06	0.05
	0.5–0.9μ	0.40	0.39	0.35	0.32	0.28	0.25	0.21	0.18
	0.9–4.0μ	0.46	0.44	0.40	0.36	0.32	0.28	0.24	0.20
ε_b		0.93	0.94	0.95	0.96	0.97	0.98	0.99	1.00

Table 3. Surface Parameters as Functions of Vegetation

Vegetation	Fig. 1a Symbol	ε_v	α_v 0.2–0.5μ	α_v 0.5–0.9μ	α_v 0.9–4.0μ	z_v m	$\sigma_{f\max}$	$\sigma_{f\max}$	$A_{c\max}$	$A_{c\min}$	$r_{c\min}$ s / m	S_{PS} W / m^2
Mixed farming, tall grassland	1	0.95	0.04	0.20	0.24	0.10	0.85	0.25	6.0	0.5	150	100
Tall / medium grassland, evergreen shrubland	2	0.97	0.05	0.25	0.30	0.05	0.80	0.70	6.0	0.8	250	100
Short grassland, meadow & shrubland	3	0.97	0.08	0.25	0.35	0.03	0.80	0.70	2.0	0.5	250	100
Evergreen forest (needleleaved)	4	0.97	0.03	0.16	0.20	0.50	0.80	0.70	6.0	5.0	250	30
Mixed deciduous, evergreen forest	5	0.98	0.03	0.24	0.30	0.40	0.80	0.60	6.0	2.0	250	30
Deciduous forest	6	0.98	0.03	0.24	0.30	0.30	0.80	0.50	6.0	1.0	250	30
Tropical evergreen broadleaved forest	7	0.98	0.03	0.16	0.20	1.00	0.90	0.80	6.0	5.0	250	30
Medium / tall grassland, woodlands	8	0.97	0.03	0.20	0.25	0.30	0.80	0.50	6.0	1.0	250	80
Tundra	9	0.97	0.04	0.21	0.25	0.01	0.40	0.30	6.0	0.5	250	50
Desert	D	0.94	0.28	0.48	0.50	0.01	0.00	0.00	0.0	0.0	0	0
Source			Briegleb et al.(1986)			Briegleb & Ramanathan (1982)			Wilson et al. (1987)			

$r_{c\max}$ is set to 5000 s / m for all vegetation types.

To define the soil color, F_i is set to 0 for white (ice), 1 for light, 2 for medium, 3 for dark and 4 for black (water) at each $1^\circ \times 1^\circ$ data cell. The resultant $\bar{F}$ is then equally divided to distinguish 8 soil colors from light (1) to dark (8). For the soil texture, F_i is assigned by clay fraction: 0 for sand (desert), 0.03 for coarse, 0.27 for intermediate, 0.60 for fine and 1 for water. The resultant mean clay fraction $\bar{F}$ is used to classify 11 soil texture classes on the basis of the Cosby et al. (1984) definition (Table 1).

The vegetation type is determined by three steps. First, the Matthews' values are grouped into 10 composite types (Table 3) according to Briegleb et al. (1986) at each $1^\circ \times 1^\circ$ data cell. The fractional area $\bar{F}$ covered by each of these composite types is then calculated from Eq.(49), where F_i is set to 1 if the specific type occurs in the given GCM grid box or 0 otherwise. And finally, the composite type which has the largest fractional coverage $\bar{F}$ is assigned to be the primary vegetation type for the GCM grid.

The geographical distributions of vegetation, soil texture and soil color types along with the continental outline are shown in Figs.1 (a–c) on the $4^\circ \times 5^\circ$ GCM grid resolution. Table 1 illustrates the soil physical parameters b, v_s, ψ_s and K_s as functions of soil texture, which are reproduced from Cosby et al. (1984). Table 2 assigns the bare soil surface terrestrial emissivity ε_b and solar albedo α_b with 3 spectral bands (1: 0.2–0.5μ; 2: 0.5–0.9μ; 3: 0.9–4.0μ) as functions of soil color. All other surface parameters which depends on vegetation types are given in Table 3.

The surface roughness lengths are determined by

$$\begin{cases} z_q = 0.2 z_0 \quad \text{for land, else} = z_0 \\ z_0 = \begin{cases} \max(z_0, z_v) & \text{for land} \\ \max(z_G, z_I) & \text{for land ice} \\ z_I & \text{for sea ice} \\ \dfrac{\alpha_{ch}}{g} C_{DN} w_a^2 & \text{for water} \end{cases} \\ z_G \equiv \min(0.041\sigma_G^{0.71}, 2) \ , \end{cases} \tag{49}$$

where $\alpha_{ch} = 0.0185$ is the Charnock coefficient (Wu 1980). $z_I = 0.25 \times 10^{-3}$ m is the roughness length for sea ice (Hanssen–Bauer and Gjessing 1988), z_G for bare ground (Hansen et al., 1983), and z_v for vegetation (Table 3). The land $z_q \propto z_0$ relation is taken from Campbell (1977). The water drag coefficient in neutral conditions C_{DN} depends on near–surface wind speed:

$$10^3 C_{DN} = \begin{cases} 1.08 w_a^{-0.15} & \text{if} \quad w_a < 2.2 \\ 0.49 + 0.065 w_a & \text{if} \quad w_a > 17.5 \\ 0.8635 + 0.043 w_a & \text{otherwise} \end{cases} \tag{50}$$

where the function for low speed is from Kondo (1975), and high speed from Large and Pond (1982), while for the middle range of wind speed, a smooth fitting between the two ends is used.

For the radiation calculations, the effective surface emissivity ε_s is defined as a linear combination of bare soil and vegetation values:

$$\varepsilon_s = \begin{cases} 1 & \text{for water, snow, ice} \\ (1 - \sigma_f)\varepsilon_b + \sigma_f \varepsilon_v & \text{for vegetated land .} \end{cases} \tag{51}$$

The effective surface albedo, however, varies with solar zenith angle, spectral band and

surface characteristics, such as vegetation, soil color, snow amount and sea ice temperature (Kiehl et al., 1987). It also differs between one for direct beam α_s and that for diffuse α_d. Over open water, α_d is set to 0.055, while α_s depends on solar zenith angle using the Briegleb et al. (1986) expression:

$$\alpha_s(\mu)=\frac{0.026}{\mu^{1.7}+0.065}+0.15(\mu-0.1)(\mu-0.5)(\mu-1)\ , \tag{52}$$

where μ is the cosine of the solar zenith angle. For all other surfaces, the effects of vegetation and snow cover are accounted by

$$\begin{cases}\alpha_x=\sigma_f\alpha'_{xv}+(1-\sigma_f)\alpha'_{xb}\\ \alpha'_{xy}=\delta_s\alpha_{xys}+(1-\delta_s)\alpha_{xy}\ ,\end{cases} \tag{53}$$

where subscript x denotes for s (direct beam) or y (diffuse), y for v (vegetation) or b (bare surface). The free–snow ice albedos depend on spectral band and surface temperature:

$$\alpha_{xy}=\begin{cases}F_{TI}(0.7,0.5,0.04,T_0) & \text{for bands } 1-2\\ F_{TI}(0.5,0.2,0.06,T_0) & \text{for band } 3\ ,\end{cases} \tag{54}$$

where $F_{TI}(a,b,c,T)\equiv\min\{a,\max[b,a-c(T-272.15)]\}$. The free–snow land albedos are functions of solar zenith angle:

$$\begin{cases}\alpha_{sy}=\alpha_y[f_\mu F_{\mu L}(0.4,\mu)+(1-f_\mu)F_{\mu L}(0.1,\mu)]\\ \alpha_{dy}=\alpha_y\ ,\end{cases} \tag{55}$$

where $F_{\mu L}(d,\mu)\equiv(1+d)/(1+2d\mu)$ following Dickinson (1983), and f_μ is the fraction of grid box with strong zenith angle dependence. Currently f_μ is set to 0 over permanent ice or 0.5 otherwise.

Snow albedos for direct beam depend on solar zenith angle following Dickinson et al. (1986):

$$\alpha_{sys}=\frac{1}{2}\left(\frac{3}{1+4\mu}-1\right)(1-\alpha_{sy})+\alpha_{sy}\ \text{ if }\ \mu<0.5,\ \text{else}=\alpha_{sy} \tag{56}$$

For diffuse, they depend on spectral band and surface temperature:

$$\alpha_{dys}=\begin{cases}F_{TI}(0.9,0.7,0.10,T_0) & \text{for bands } 1-2\\ F_{TI}(0.6,0.3,0.15,T_0) & \text{for band } 3\ .\end{cases} \tag{57}$$

Parameters σ_f and A_c depend on vegetation type as well as the time of the year. They are now interpolated from their corresponding summer (maximum) and winter (minimum) values in Table 3:

$$\begin{bmatrix}\sigma_f\\ A_c\end{bmatrix}=f_{d\mu}\begin{bmatrix}\sigma_f\\ A_c\end{bmatrix}_{\max}+(1-f_{d\mu})\begin{bmatrix}\sigma_f\\ A_c\end{bmatrix}_{\min}\ , \tag{58}$$

where $f_{d\mu}$ is the ratio of the local daily mean μ to the corresponding summer value.

The reference temperature T_r can be prescribed as follows. Integrating Eq.(5) over entire seasonal cycles of sufficient years, and assuming tendency terms and G for this time period to be zero, we have

$$\begin{cases}(a_s-b_s)T_r+b_s\overline{T}_m=a_s\overline{T}_0\\ (a_m-b_m)T_r-a_m\overline{T}_m=-b_m\overline{T}_0\end{cases} \tag{59}$$

This results in $T_r = \overline{T}_0$. Therefore, T_r is prescribed as the long-term annual mean distribution of observed surface temperature.

The distributions of sea-surface temperature and sea ice cover on the GCM global grid are currently prescribed from the monthly data of Alexander and Mobley (1976). The sea-surface temperature are updated at the end of each day by linear interpolation of the consecutive monthly mean values. The sea ice distribution is changed accordingly. When a grid box changes from open ocean to sea ice, the initial surface temperature is set to 0°C. And when it changes from sea ice to open ocean, the surface snow mass is set to zero.

V. CLIMATE SIMULATIONS

The final version of the GCM was frozen in September 1990. Due to the constraint of time and the computational resource, very preliminary tuning of the model toward the representation of the present climate had been applied. The model was continuously integrated for a 2.5-year period, and the result presented below is from the final January and July monthly means.

Table 4 illustrates the GCM simulated versus observed global means. When the 1986-88 averaged ERBE data are compared and for clear-sky conditions, the model emits slightly less outgoing longwave radiation (by 4 W/m^2 in January and 3 W/m^2 in July) and produces a smaller planetary albedo (by 2% in January and 1% in July). This is associated with an overall cooler air temperature and a higher surface albedo. In cloudy conditions, the model somewhat overestimates outgoing longwave radiation and underestimates planetary albedo. Thus, the GCM cloud radiative forcing is weaker than the observed for both solar and terrestrial radiations. This is consistent with the fact that the model generates systematically smaller cloud cover than the ISCCP data. Surface air temperature is overall cooler in the model (by 0.6°C in January and 0.5°C in July) when the Schutz and Gates (1971, 1972) data are compared. Precipitation is larger in January and smaller in July as compared with the Jaeger (1976) data. A similar bias occurs in atmospheric moisture content (i.e., precipitable water) when the Trenberth et al. (1987) data are compared. Note that all above model errors are within observed data uncertainties and, hence, are considered to be small.

Table 4. Comparison of GCM Simulated January and July Global Means with Observation

Climate Variables		January		July		Observation Source
		GCM	*OBS*	*GCM*	*OBS*	
Outgoing LW Radiation (W/m^2)	Clear	257	261	265	268	ERBE 1986-88
	Total	234	233	241	239	
Planetary Albedo (%)	Clear	17	19	15	16	
	Total	31	33	31	31	
Cloud Radiative Forcing (W/m^2)	LW	23	28	24	29	
	SW	−47	−53	−43	−51	
	Net	−24	−25	−19	−22	
Total Cloud Cover (%)		52	62	51	63	ISCCP 1986-88
Precipitable Water (g/cm^2)		2.50	2.47	2.72	2.80	Trenberth et al. 1987
Precipitation Rate (mm / day)		2.69	2.59	2.76	2.77	Jaeger 1976
Surface Air Temperature (°C)		11.6	12.2	15.6	16.1	Schutz & Gates 1971, 72

Figures 2 (a-c) show the GCM simulated versus observed zonal mean distributions of

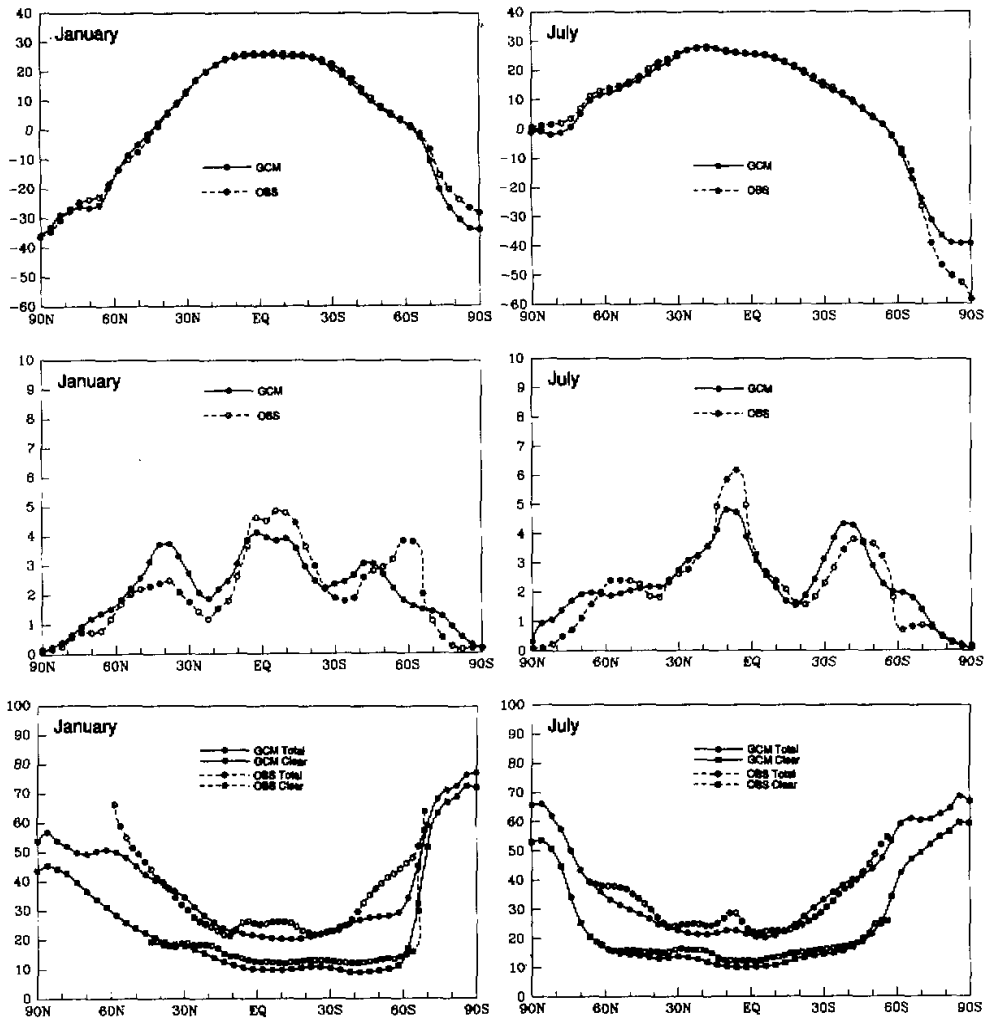

Fig. 2. GCM simulated versus observed January and July zonal mean distributions of:a) surface air temperature (°C), b) precipitation rate (mm / day), and c) planetary albedo (%) for clear / cloudy conditions. the observations are from Schutz and Gates (1971, 1972), Jaeger (1976) and 1986–1988 averaged ERBE data, respectively.

surface air temperature, precipitation and planetary albedo. Clearly, the observed (Schutz and Gates, 1971, 1972) meridional structure of surface air temperature is well reproduced by the model. The temperature errors are generally less than 3° except in the south polar region, where the model is about 5° cooler in January and 5–15° warmer in July. This may indicate that the current ice surface parameterization requires further improvement. In addition, the model is systematically cooler by $\sim 1°$ in the summer extratropics. This warrants a refined tuning of parameter prescriptions (such as D_a) used to determine T_a.

The GCM simulates reasonably well major observed (Jaeger, 1976) precipitation features. For example, the model correctly represents the seasonal migration of ITCZ as well

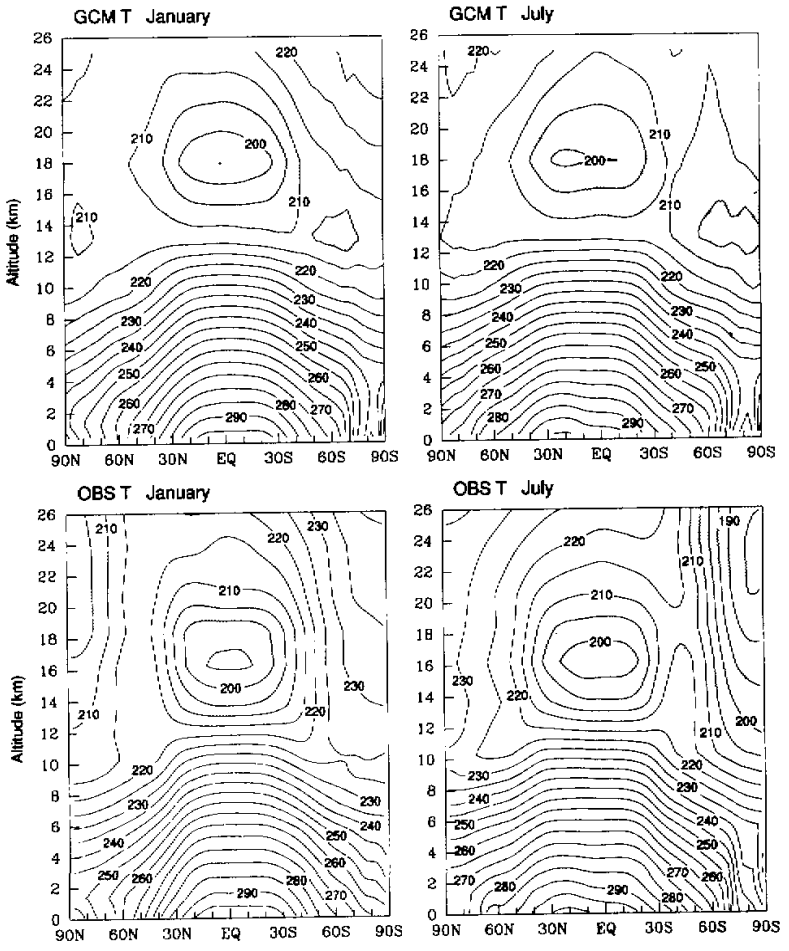

Fig. 3. GCM simulated versus observed (Trenberth, 1992) vertical distributions of January and July zonal mean temperature. Contour intervals are 5 K, and shadings indicate the area of temperatures cooler than 210 K.

as its associated northern and southern Hadley circulations. Two systematic biases, however, are identified in both January and July. First, the model tropical rainfall is ~ 1 mm / day smaller than observations. This suggests that our first choice of the prescribed evaporation rate (20 percent) for convective rainfall is too large and shall be appreciatively reduced. For the future, this problem shall be addressed more preferably by incorporating a physically based parameterization of downdraft into the convection scheme. Second, the southern mid–latitude precipitation features are shifted to the north of observations. This shift is likely resulted from errors in the model dynamics. A similar northward shift is identified in sea–level pressure (not shown) and the mid–latitude westerly jet (see below). Preliminary experiments show that this error is sensitive to the specification of the dynamic "flexible coefficients" in the energy conversion terms.

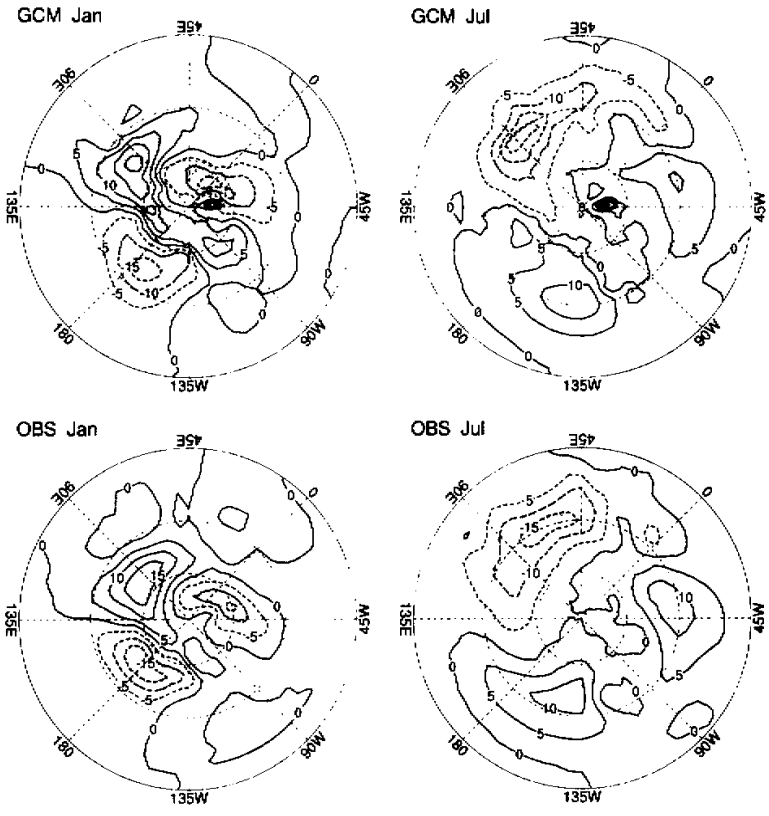

Fig. 4. GCM simulated versus observed (Schutz and Gates, 1971; 1972) geographic distributions of January and July sea-level pressure eddies. Contour intervals are 5 hPa, and negative values are dashed. The light (denes) shadings indicate the area of pressures higher (lower) than +10(−10) hPa.

The GCM clear-sky planetary albedo distribution follows well the ERBE data except for a general underestimation over low- and mid-latitudes. If the ERBE data are taken as the "truth", a modification is then needed to increase surface albedo, especially over oceans. For cloudy conditions, the discrepancy of planetary albedo results mainly from that of cloud cover. For example, the GCM generates a smaller cloud amount associated with ITCZ for both January and July. This is a result of less model convective precipitation discussed above. [Recall that the convective cloud amount, which dominates the ITCZ region, is parameterized in terms of precipitation rate (see **Cloud Formation**).] Over the mid-latitudes, such as near 50°N of January / July and 50°S of January, the model albedo is smaller than the ERBE data. This is identified with insufficient model stratiform cloud as compared with the ISCCP data. Currently, the model stratiform cloud forms in a single prognostic layer within each of three vertical domains (see **Cloud Formation**). This constraint is likely responsible for the

insufficient cloud amount just indicated and, thus, shall be eliminated in the future. Nevertheless, it is more preferable to have a continuous spatial coverage of clouds.

Figure 3 depicts the GCM simulated versus observed (Trenberth, 1992) vertical distributions of zonal mean temperature. One obvious feature is that, over high latitudes, large cold biases occur in the upper troposphere and lower stratosphere for both January and July. This deficiency is common in most current GCMs (Boer et al., 1991). Increasing horizontal resolution may not necessarily reduce such cold biases (Boer et al., 1991; Liang et al., 1996). In these regions, however, the ozone effect may play an important role (Liang and Wang, 1995). In addition, preliminary experiments indicate that these biases are sensitive to the specification of the dynamic "flexible coefficients" in the energy conversion terms. Therefore, improvement can be achieved by both a better representation of model physics and a more accurate model dynamics. The large temperature gradient errors cause the Southern Hemispheric westerly jet to shift to the north of observations (not shown). For the same reason, the model produces unrealistically weaker stratospheric polar westerly jets in the winter hemisphere. This deficiency, however, may also be a result of insufficient vertical resolution for the model stratosphere.

Figure 4 presents the GCM simulated versus observed (Schutz and Gates, 1971; 1972) geographic distributions of sea–level pressure eddy structure where zonal means are removed. The principal eddy structures in the Northern Hemisphere are realistically simulated. These include Aleutian low, Icelandic low, Siberian high and North American high in January, North Pacific high, North Atlantic high and Asian monsoon low in July. The most notable model deficiency is that the July Asian monsoon low is shifted to the east of observations by $\sim 20^{\circ}$. In addition, the model tends to overestimate the strength of the Eurasia continental systems (January Siberian high and July Asian monsoon low). This may suggest the need for a more comprehensive treatment of topographic effects in terms of both dynamic and thermal forcings.

In all circumstances, the preliminary GCM climate simulations have shown very encouraging results. The current version of the model, however, is not perfect and warrants further refinements. Several notable deficiencies have been identified above along with possible areas that needs improvement. Others may be revealed in the future after conducting more simulations and detail diagnoses.

I wish to express my most sincere thanks to Prof. Qing–Cun Zeng, who provided me with the opportunity, inspiration and confidence without which I could not have fulfilled this research. I am grateful to Prof. Robert D. Cess and appreciate his generous support, both academic and personal, during my visit in SUNY at Stony Brook. My heartfelt thanks go to Prof. Xue–Hong Zhang for his wonderful professional partnership, continual encouragement and friendship. My thanks must also extend to Dr. Jeffrey T. Kiehl who kindly provided me with the NCAR CCM1 radiation source code, to Prof. David A. Randall with the Arakawa–Schubert convection source code, and to Dr. Roy L. Jenne with the NCAR archived surface boundary data.

This research was jointly supported by the CO_2 Research Division, Office of Basic Energy Sciences, U.S. Department of Energy, under Grant DEFG0285ER60314 to SUNY at Stony Brook, and the Laboratory of Numerical Modeling for Atmospheric Sciences and Geophysical Fluid Dynamics, Institute of Atmospheric Physics, Chinese Academy of Sciences.

REFERENCES

Albrecht, B.A., V. Ramanathan, and A. Boville (1986), The effects of cumulus moisture transports on the simulation of climate with a general circulation model, *J. Atmos. Sci.*, **43:** 2443–2462.

Alexander, R.C., and R.L. Mobley (1976), Monthly average sea–surface temperatures and ice–pack limits on a 1° global grid, *Mon. Wea. Rev.*, **104:** 143–148.

Arakawa, A. (1972), Design of the UCLA general circulation model, Tech. Report No. 7, Department of Meteorology, University of California, Los Angeles, 116 pp.

Arakawa, A., and W.H. Schubert (1974), Interaction of a cumulus cloud ensemble with the large scale environment, Part I, *J. Atmos. Sci.*, **31:** 674–701.

Boer, G.J., K.Arpe, M.Blackburn, M.Deque, W.L. Gates, T.L. Hart, H.le Treut, E.Roeckner, D.A. Sheinin, I. Simmonds, R.N.B. Smith, T.Tokioka, R.T. Wetherald and D.Williamson (1991), *An Intercomparison of the Climates Simulated by 14 Atmospheric General Circulation Models*, WMO / TD–No. 425, World Met. Organiz., Geneva, 37 pp.

Boer, G.J., N.A. McFarlane, R. Laprise, J.D. Henderson, and J.–P.Blanchet (1984), The Canadian Climate Centre spectral atmospheric general circulation model, *Atmos.–Ocean*, **22:** 397–429.

Bourke, W. (1974), A multi–level spectral model, I: Formulation and hemispheric integrations, *Mon. Wea. Rev.*, **102:** 687–701.

Briegleb, B.P., P. Minnis, V. Ramanathan, and E. Harrison (1986), Comparison of regional clear–sky albedos inferred from satellite observations and model computations, *J. Clim. Appl. Meteorol.*, **25:** 214–226.

Briegleb, B., and V. Ramanathan (1982), Spectral and diurnal variations in clear sky planetary albedo, *J. Appl. Meteorol.*, **21:** 1160–1171.

Campbell, G.S. (1977), An Introduction to Environmental Biophysics, Springer–Verlag, 159 pp.

Clapp, R., and G. Hornberger (1978), Empirical equations for some soil hydraulic properties, *Water Resour. Res.*, **14:** 601–609.

Cosby, B.J., G.M. Hornberger, R.B. Clapp, and T.R. Ginn (1984), A statistical exploration of the relationships of soil moisture characteristics to the physical properties of soils, *Water Resour. Res.*, **20:** 682–690.

Deardoff, J.W. (1967), Dependence of the eddy coefficient for heat upon stability above the lowest 50 m, *J. Appl. Meteorol.*, **6:** 631–643.

Delage, Y. (1986), Surface temperature calculation in atmospheric circulation models with coarse resolution of the boundary layer, *Mon. Wea. Rev.*, **114:** 442–451.

Dickinson, R.E. (1983), Land surface processes and climate— Surface albedos and energy balance, *Advances in Geophysics*, **25:** 305–353.

Dickinson, R.E. (1984), Modeling evaportranspiration for three–dimensional global climate models, In Climate Processes and Climate Sensitivity, J.E. Hansen and K. Takahashi (Eds.), *Geophysical Monograph*, **29:** pp 58–72.

Dickinson, R.E., A. Henderson–Sellers, P.J. Kennedy, and M.F. Wilson (1986), *Biosphere–Atmosphere Transfer Scheme (BATS) for the NCAR Community Climate Model*, NCAR Tech. Note, NCAR / TN–275+STR, National Center for Atmospheric Research, Boulder, CO.

Dyer, A.J., and E.F. Bradley (1982), An alternative analysis of flux–gradient relationships at the 1976 ITCE, *Boundary–Layer Meteorol.*, **22:** 3–19.

Hansen, J., G. Russell, D.Rind, P.Stone, A.Lacis, S.Lebedeff, R.Ruedy, and L.Travis (1983), Efficient three–dimensional global models for climate studies: Models I and II, *Mon. Wea. Rev.*, **111:** 609–662.

Hanssen–Bauer, I., and Y.T. Gjessing (1988), Observations and model calculations of aerodynamic drag on sea ice in the Fram Strait, *Tellus*, **40A:** 151–161.

Harshvardhan, D.A. Randall, T.G. Corsetti, and D.A. Dazlich (1989), Earth radiation budget and cloudiness simulations with a general circulation model, *J. Atmos. Sci.*, **40:** 1922–1942.

Hoestroem, U. (1985), Von Karman constant in atmospheric boundary layer flow: reevaluated, *J. Atmos. Sci.*, **42:** 263–270.

Jacobsen, I., and E. Heise (1982), A new economic method for the computation of the surface temperature in numerical models, *Beitr. Phys. Atmosph.*, **55**(2): 128–141.

Jaeger, L. (1976), Montatskarten des Niederschlages fur die ganze Erde, *Ber. Dtsch. Wetterienst*, **18:** 38 pp.

Joseph. D. (1980), *Navy 10' Global Elevation Values*, NCAR Tech. Note, National Center for Atmospheric Research, Boulder, CO.

Kiehl, J.T., and B.P. Briegleb (1991), A new parameterization of the absorptance due to the 15 micron band system of carbon dioxide, *J. Geophys. Res.*, **96:** 9013–9019.

Kiehl, J.T., R.J. Wolski, B.P. Briegleb, and V. Ramanathan (1987), *Documentation of radiation and cloud routines in the NCAR Community Climate Model (CCM1)*, NCAR Tech. Note, NCAR / TN–288+1A, National Center for Atmospheric Research, Boulder, CO.

Kiehl, J.T., and T. Yamanouchi (1985), A parameterization for absorption due to the A, B, and gamma oxygen bands, *Tellus*, **37B:** 1–6.

Kondo, J. (1975), Air–sea bulk transfer coefficients in diabatic conditions, *Boundary–Layer Meteorol.*, **9:** 91–112.

Kratz, D.P., and R.D. Cess (1985), Solar absorption by atmospheric water vapor: A comparison of radiation models, *Tellus*, **37B:** 53–63.

Lacis, A.A., and J.E. Hansen (1974), A parameterization for the absorption of solar radiation in the Earths atmosphere, *J. Atmos. Sci.*, **31:** 118–133.

Large, W.G., and S. Pond (1982), Sensible and latent heat flux measurement over ocean, *J. Phys. Oceanogr.*, **12:** 464–482.

Liang, X.–Z. (1986), The Design of IAP GCM and the Simulation of Climate and Its Interseasonal Variability, *Ph.D. Dissertation*, Institute of Atmospheric Physics, Chinese Academy of Sciences, 250 pp.

Liang, X.–Z. and W.–C. Wang (1995), A GCM study of the climatic effect of 1979–1992 ozone trend, In *Atmospheric Ozone as a Climate Gas*, NATO ASI Series, W.–C. Wang and I.S.A. Isaksen (Eds.), pp. 259–288.

Liang, X.–Z., W.–C. Wang, A. N. Samel, D. Pollard, and S.L. Thompson (1996), Systematic biases of SUNYA / NCAR AMIP simulations. In *Proceedings of First International AMIP Scientific Conference, WCRP Report* (**to appear**).

Lord, S.J. (1978), Development and observational verification of a cumulus cloud parameterization, *Ph.D Dissertation*, University of California, Los Angeles, 339 pp.

Lord, S.J., W.C. Chao, and A. Arakawa (1982), Interaction of a cumulus cloud ensemble with the large–scale environment, Part IV: The discrete model, *J. Atmos. Sci.*, **39:** 104–113.

Mahrt, L., and H.–L. Pan (1984), A two–layer model of soil hydrology, *Boundary–Layer Meteorol.*, **29:** 1–20.

Manabe, S., J. Smagorinsky, and R.F. Strickler (1965), Simulated climatology of a general circulation model with a hydrologic cycle, *Mon. Wea. Rev.*, **93:** 769–798.

Matthews, E. (1983), Global vegetation and land use: New high–resolution data bases for climate studies, *J. Clim. Appl. Meteorol.*, **22:** 474–487.

McCumber, M.C., and R.A. Pielke (1981), Simulation of the effects of surface fluxes of heat and moisture in a mesoscale numerical model, 1. Soil layer, *J. Geophys. Res.*, **86:** 9929–9938.

Miyakoda, K., and J. Sirutis (1986), Manual of the E–Physics, [Available from the Geophysical Fluid Dynamics Laboratory, Princeton University, P.O. Box 308, Princeton, NJ 08542.]

Nieuwstadt, F.T.M., and H. Tennekes (1981), A rate equation for the nocturnal boundary layer height, *J. Atmos. Sci.*, **38:** 1418–1428.

Noilhan, J., and S. Planton (1989), A simple parameterization of land surface processes for meteorological models, *Mon. Wea. Rev.*, **117:** 536–549.

Palmer, T.N., G.J. Shutts, and R. Swinbank (1986), Alleviation of a systematic westerly bias in general circulation and numerical weather prediction models through an orographic gravity wave drag parameterization, *Quart. J. Roy. Meter. Soc.*, **112:** 1001–1039.

Pan, H.–L., and L. Mahrt (1987), Interaction between soil hydrology and boundary–layer development, *Boundary–Layer Meteorol.*, **38:** 185–202.

Philip, J.R. (1987), A physical bound on the Bowen ratio, *J. Clim. Appl. Meteorol.*, **26:** 1043–1045.

Priestley, C.H.B. (1959), Turbulent Transfer in the Lower Atmosphere, The University of Chicago Press, Chicago, IL, 130 pp.

Ramanathan, V., and R.E. Dickinson (1979), The role of stratospheric ozone in the zonal and seasonal radiative energy balance of the Earth–troposphere system, *J. Atmos. Sci.*, **36:** 1084–1104.

Ramanathan, V., and P. Downey (1986), A nonisothermal emissivity and absorptivity formulation for water vapor, *J. Geophys. Res.*, **91:** 8649–8666.

Ramanathan, V., E.J. Pitcher, R.C. Malone, and M.L. Blackmon (1983), The response of a spectral general circulation model to refinements in radiative processes, *J. Atmos. Sci.*, **40:** 605–630.

Sasamori, T., J. London, and D.V. Hoyt (1972), Radiation budget of the Southern Hemisphere, *Meteorological Monographs*, **35**, American Meteorological Society, Boston, MA, 9–22.

Schlesinger, M.E., and J.–H. Oh (1988), A parameterization of the evaporation of rainfall, *Mon. Wea. Rev.*, **116:** 1887–1895.

Schutz, C., and W.L. Gates (1971), Global climate data for surface, 800 mb, 400 mb: January, R–915–ARPA, 173 pp.

Schutz, C., and W.L. Gates (1972), Global climate data for surface, 800 mb, 400 mb: July, R–1029–ARPA, 180 pp.

Slingo, J.M. (1987), The development and verification of a cloud prediction scheme for the ECMWF model, *Quart. J. Roy. Meteor. Soc.*, **113:** 899–927.

Smolarkiewicz, P.K., and W.W. Grabowski (1990), The multidimensional positive definite advection transport algorithm: Nonoscillatory option, *J. Comput. Phys.*, **86:** 355–375.

Trenberth, K.E. (1992), *Global Analyses from ECMWF and Atlas of 1000 to 10 mb Circulation Statistics*, NCAR Tech. Note, NCAR / TN–373+STR, National Center for Atmospheric Research, Boulder, CO., 191 pp.

Trenberth, K.E., J.R. Christy, and J.G. Olson (1987), Global atmospheric mass, surface pressure, and water vapor variations, *J. Geophys. Res.*, **92:** 14815–14826.

Wetzel, P.J., and J.–T. Chang (1987), Concerning the relationship between evapotranspiration and soil moisture, *J. Clim. Appl. Meteorol.*, **26:** 18–27.

Wilson, M.F., and A. Henderson–Sellers (1985), A global archive of land cover and soils data for use in general circulation climate models, *J. Climatol.*, **5:** 119–143.

Wilson, M.F., A. Henderson–Sellers, R.E. Dickinson, and P.J. Kennedy (1987), Investigation of the sensitivity of the land–surface parameterization of the NCAR Community Climate Model in regions of tundra vegetation, *J. Climatol.*, **7:** 319–343.

Wu, J. (1980), Wind-stress coefficients over sea surface near neutral conditions —A revisit, *J. Phys. Oceanogr.*, **10**: 727–740.

Zeng, Q.-C. (1983), Some numerical ocean-atmosphere coupling models, *In Proceedings of the First International Symposium on the Integrated Global Ocean Monitoring* (Tallinn, USSR, October 2–10).

Zeng, Q.-C., C.-G. Yuan, X.-H. Zhang, X.-Z. Liang and N. Bao (1987), A global grid-point general circulation model, In Collection of Papers Presented at the WMO / IUGG NWP Symposium (Tokyo, August 4–8, 1986), pp. 421–430.

Zeng, Q.-C., X.-H. Zhang, X.-Z. Liang, C.-G. Yuan and S.-F. Chen (1989), Documentation of IAP Two-Level Atmospheric General Circulation Model, DOE / ER / 60314-H1, TRO44, 383 pp.

Zhang, X.-H. (1990), Dynamical framework of IAP nine-level atmospheric general circulation model, *Advances in Atmospheric Sciences*, 7(1): 66–77.